ISEIS

Journal of Environmental Informatics Letters 7(2) 90-102 (2022)

Journal of Environmental Informatics Letters

www.iseis.org/jeil

# Coupled Hydraulic-Thermal Model for Soils under Extreme Weather in Cold Regions

R. Paranthaman[1] and S. Azam[1 *]

[1] *Environmental Systems Engineering, Faculty of Engineering and Applied Science, University of Regina, 3737, Wascana Parkway, Regina, SK S4S 0A2, Canada*

Received 24 May 2022; revised 15 June 2022; accepted 19 June 2022; published online 30 June 2022

**ABSTRACT.** Extreme weather conditions govern the hydraulic and thermal properties of glacial clay deposits under the cold climate of the Canadian Prairies. The prediction of time-dependent soil behavior over the entire year and under extreme weather conditions is required for the design and construction of buried infrastructure. The main contributions of this research are the development and validation of a coupled soil-atmosphere interaction model to predict transient water and heat movement under mean, extreme dry, and extreme wet weather scenarios. Results indicated that the hydraulic properties are governed by the net water flux that resulted in the shifting of the seasons as follows: mean that comprises winter (3½ months), spring (1 month), summer (5½ months), and fall (2 months); dry that includes spring (4 months), summer (4 months), and fall (4 months); and wet that has winter (4 months), inseparable spring-summer (5 months), and fall (3 months). The thermal properties are governed by air temperature for the investigated soil. Identical values of thermal gradient during spring-summer (April to October) in all scenarios indicate that the soil gains more heat compared with the heat loss during fall-winter (November to March), especially for mean and dry conditions. Furthermore, the inflection points in heat flux show that the soil gains heat from May to August and loses heat from September to April. Finally, the active depth of soil was found to be 4 ± 1 m for hydraulic properties and 3 m for heat flux.

*Keywords:* climate interaction, hydraulic flow, thermal flow, numerical modeling

## 1. Introduction

The Canadian Prairies provide a challenging environment in terms of glacially evolved clay deposits in a predominantly cold climate with extensive seasonal variations (Azam et al., 2013; Paranthaman and Azam, 2021a). These soils support buried pipelines (for water, oil, gas, or heat) that are generally installed within a few meters from the ground surface. Failure of such pipeline networks is routinely reported from across the region. For example, water main breaks of 6,381 in 2,692 km during 2005 ~ 2015 in Winnipeg (City of Winnipeg, 2022), 2,430 in 900 km during 1995 ~ 2004 in Regina (Hu et al., 2008; City of Regina, 2022), and 4,400 in 3,800 km during 2005 ~ 2015 in Edmonton (Teslak, 2018). Such damages occur in all pipe sizes (12 to 200 mm) and all pipe materials (asbestos cement, cast iron, and polyvinyl chloride) (Hu and Vu, 2006, 2011; City of Winnipeg, 2022). Distress in the linear infrastructure systems is derived from coupled hydraulic and thermal processes in the surface soils (Newport, 1981; Rajani et al., 2012). Cyclic precipitation-evaporation during spring-summer-fall as well as freeze-thaw during the fall-winter-spring result in ground deformation and slope instability. Furthermore, extreme weather events such as flash-floods and long-droughts have been observed throughout the region and are attributed to the adverse effects of climate change (Bonsal et al., 2017; Akhter and Azam, 2019). Such uncertainties of seasonal weather impose serious concerns on the efficiency of buried utilities (Kleiner and Rajani, 2002; Yang and Wang, 2019).

Failures in buried pipelines are due to increased stresses derived from two distinct soil-atmosphere interaction mechanisms: saturation-desaturation, due to alternate precipitation and evaporation, which results in swelling and shrinkage in clayey soils (Kleiner and Rajani, 2002) and freeze-thaw, due to seasonal temperature variations, that results in 10% volume expansion during ice lens formation and localized shear strength reduction during ice melt (Hu and Vu, 2011). Over time, these hydraulic and thermal processes occur repeatedly and increase the size of pore spaces within the clay matrix (Tripathy and Subba Rao, 2009) as well as micro-level cracks in the bulk soil (Ito et al., 2022). These features facilitate the flow of air, water, heat, and contaminants through the soil thereby further aggravating the integrity of buried pipes. Clearly, such transient mechanisms are related to both hydraulic and thermal flows and, in turn, are governed by soil properties and regional climatic conditions.

* Corresponding author. Tel.: +1 306-337-2369; fax: +1 306-585-4855.
*E-mail address:* shahid.azam@uregina.ca (S. Azam).

ISSN: 1726-2135 print/1684-8799 online
 doi:10.3808/jeil.202200082

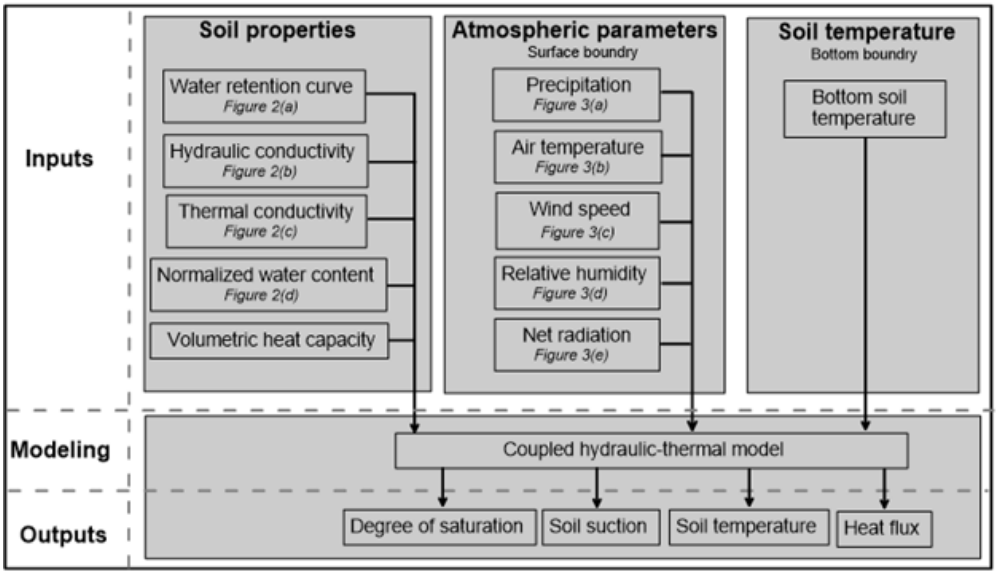


**Figure 1.** Modeling procedure for coupled hydraulic-thermal model.

Water and heat flows through soils are derived from complex soil-atmospheric interactions. During evaporation, the hydraulic flow is upwards in a soil profile because of soil suction due to capillary action at the air-water interface within the soil pores (Hillel, 1998). When the soil is significantly dry, the adsorbed water on clay minerals can also be removed through vaporization (Mitchell and Soga, 2005). In contrast, hydraulic flow is downwards during precipitation as water replaces air within the soil pores (Lu and Likos, 2004). In this case, the soil depth up to the advancing water front is considered to be saturated, that is, all soil pores are filled with water (Green and Ampt, 1911). Likewise, periodic freeze-thaw is related to temporal heat changes in the atmosphere that are gradually transferred through the surface layer during saturation and desaturation (Nowamooz et al., 2016; Le et al., 2020). Thermal recharge is provided by solar radiation from the surface downwards and deeper soil layers in the upward direction (Tissen et al., 2019). Heat flow primarily occurs by conduction through clay particles when the soil is completely dry and through the particles, pore water, and pore ice when the soil is fully saturated (Newman and Wilson, 1997; Côté and Konrad, 2005).

The hydraulic and thermal behaviors of soils in cold regions have been widely investigated using coupled flow models. The initial mathematical formulations were developed by accounting for latent heat during phase changes and water migration from the soil matrix to the freezing front (Harlan, 1973; Taylor and Luthin, 1978; Fukuda et al., 1980). The analytical equations were subsequently improved to include the volume of water and ice (Konrad and Morgenstern, 1984; Nixon, 1991). The use of the finite element method in computer codes increased the utility of such models by reducing processing time and increasing mathematical accuracy (Padilla and Villeneuve, 1992; Qin et al., 2021). These models were further upgraded to include soil property functions (Newman and Wilson, 1997; Dall'Amico et al., 2011), temperature variations through the profile (Tan et al., 2011; Qin et al., 2021), and vapor flow during saturation-desaturation (Vitel et al., 2016; Huang et al., 2018). Generally, the numerical models are used to mimic routine atmospheric conditions during fall-winter. To the authors' knowledge, the prediction of transient soil behavior over the entire year and under extreme weather conditions is not investigated.

The main objective of this paper is to assess the transient hydraulic and thermal properties of soils under extreme weather in cold climates. A coupled hydraulic-thermal model was developed using a typical clayey soil and the atmospheric parameters from Saskatchewan, Canada. Results were validated with measured mean soil temperature from a monitoring station (latitude of 52°09'N, longitude of 106°36'W and elevation of 497 m above sea level). The variation of hydraulic and thermal properties at shallow depths was predicted under mean and extreme weather.

## 2. Governing Equations

Fluid flow (water and vapor migration) occurs through soil pores due to water flux. Considering an incompressible water phase and negligible soil volume changes, transient volumetric water content ($\partial\theta_w$ / $\partial t$, 1/day) is determined by combining Darcy's law (water gradient) and Fick's law (vapor gradient), as shown in the following equation (Geostudio, 2020):

$$\frac{\partial\theta_w}{\partial t} = \frac{k_u}{dy}\left(\frac{\partial\psi}{g\partial y\rho_w}+1\right)+\frac{D_v\partial\psi}{dy\partial y\rho_w}-\frac{M\partial}{\rho_w R\partial t}\left(\frac{p_v\theta_a}{T}\right) \quad (1)$$

In the above equation, $k_u$ is hydraulic conductivity (m/day), $g$ is the gravitational acceleration (m/s$^2$), $\psi$ is soil suction (kPa), $\rho_w$ is water density (kg/m$^3$), $D_v$ is vapor diffusivity (day), $M$ is vapor molar mass (kg/mol), $R$ is the universal gas constant (8.314 J/(K·mol), $T$ is soil temperature (K), $p_v$ is vapor pressure

(kPa), and $\theta_a$ is volumetric air content.

For use in Equation 1, the net water flux ($q_i$, m/day) is derived from measured precipitation ($q_p$, m/day) and actual evaporation ($q_{AE}$, m/day) that, in turn, is estimated using the following equation (Wilson et al., 1997):

$$q_{AE} = \frac{\Gamma q_n h_s h_a + 0.1746\rho_{vs}(1+0.146U_a)(h_s - h_a)}{h_a(\Gamma h_s + 0.0665)} \quad (2)$$

In the above equation, $\Gamma$ is the slope of the saturation vapor pressure versus temperature curve (kPa/°C), $q_n$ is net radiation (m/day), $U_a$ is wind speed (m/day), $p_{vs}$ is saturated vapor pressure (mm Hg), $h_a$ is relative humidity of air, and $h_s$ is relative humidity of soil. Details on the determination of $\Gamma$ and $p_{vs}$ are given in Lowe (1977) and of $h_s$ in Bittelli et al. (2015). Finally, the surface runoff ($q_R$, m/day) is calculated from mass balance.

Thermal flow (heat conduction) occurs through solid particles, pore water, and pore ice due to heat flux. The transient temperature ($\partial T / \partial t$, K/day) is determined by the following form of the Fourier's law (Geostudio, 2020):

$$\frac{\partial T}{\partial t} = \left[\frac{\partial}{\partial y}\left(K_T \frac{\partial T}{\partial y}\right) - h_v \frac{\partial m_v}{\partial y \partial t}\right] / \left(C_p + \rho_w h_f \frac{\partial \theta_w}{\partial T}\right) \quad (3)$$

In the above equation, $K_T$ is the thermal conductivity of soil (J/(s·m·K)), $h_v$ is the latent heat of vaporization (kJ/kg), ($\partial m_v / \partial t$) is the vapor mass flow rate per area (kg/(m$^2$·day)), $C_p$ is the volumetric heat capacity (J/(m$^3$·K)), $h_f$ is the latent heat of condensation (kJ/kg), and ($\partial \theta_w / \partial T$) is the slope of volumetric water content and temperature (1/K).

For use in Equation 3, the net heat flux ($q_g$, m/day) is derived from measured net radiation, estimated sensible heat ($q_s$, m/day), and estimated latent heat ($q_l$, m/day). The energy balance is determined by integrating the atmospheric parameters and soil properties, as shown in the following equation (Wilson, 1990; Geostudio, 2020):

$$q_g = q_n - \left[3.142(1+0.146U_a)(T_s - T_a)\right] - \left(\frac{q_{AE}\rho_w h_v}{1000}\right) \quad (4)$$

In the above relationship, $T_s$ is soil temperature (°C) and $T_a$ is air temperature (°C). For use in the equation, the units of $q_g$ were converted from m/day to kJ/(m$^2$·day) by multiplying the $q_g$ with $h_v$ and $\rho_w$ (Wilson, 1990).

## 3. Model Development

Figure 1 describes the modeling procedure of the coupled hydraulic-thermal model. A one-dimensional model was developed to simplify calculations and reduce computational time. An 8 m deep soil column with 10 mm vertical elements was used to minimize water balance error. Each element was assigned the soil properties: water retention curve (WRC), hydraulic conductivity curve (HCC), normalized volumetric water content, thermal conductivity curve, and volumetric heat capacity. The initial condition of the soil column was selected to be at the optimum state: $w$ = 14% and $\gamma_d$ = 18.3 kN/m$^3$ that corresponded to $\theta_w$ = 33% and $S$ = 80% (Paranthaman and Azam, 2021b). At the surface of the soil column, the following atmospheric parameters were assigned: precipitation, air temperature, wind speed, relative humidity, and net radiation. In contrast, only the soil temperature was assigned at the bottom of the soil column.

As described later in this paper, atmospheric conditions pertaining to extreme dry, mean, and extreme wet weather were simulated over a one-year period. The partial differential equations were solved by the finite element method using a comercial software (GEO Studio - Seep/W module). The water content values obtained from the hydraulic equation (1) were used in the thermal equation (3) thereby accounting for the effect of soil partial saturation on thermal movement into the soil column. The model results were plotted in the form of degree of saturation ($S$) and soil suction ($\psi$) as well as soil temperature and heat flux as functions with respect to both time and depth.

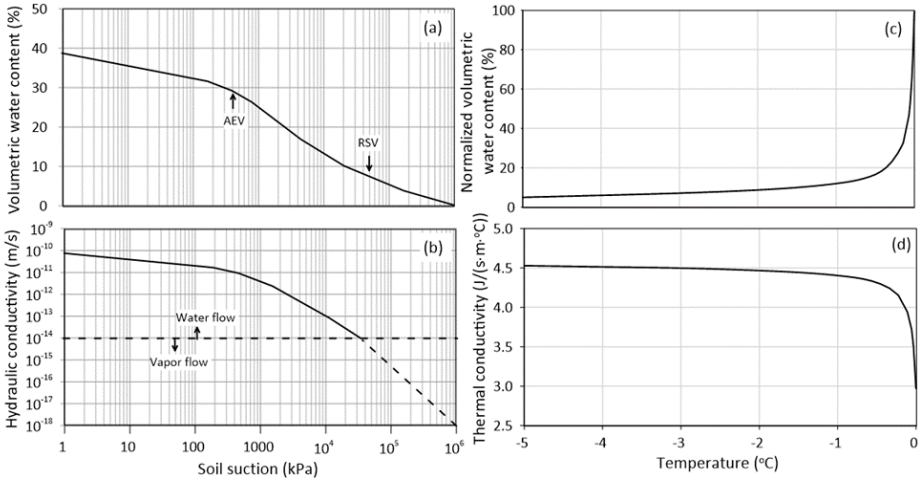


**Figure 2.** Soil properties: (a) water retention curve; (b) hydraulic conductivity curve; (c) normalized volumetric water content; and (d) thermal conductivity curve.

### 3.1. Soil Properties

A typical clay with a specific gravity of 2.72 and containing 18% clay size fraction (material finer than 0.002 mm) was used. According to Paranthaman and Azam (2021a), this material constitutes quartz (82%), clays minerals (9%), and carbonate minerals (9%). Figure 2 gives the soil properties of the investigated clay. The laboratory determined WRC (Figure 2a) by Paranthaman and Azam (2021b) was fitted using the following equation (Fredlund and Xing, 1994):

$$\theta_w = \theta_s \left\{ \frac{1}{ln\left[2.718 + \left(\frac{\psi}{a}\right)^n\right]^m} \right\} \left[ \frac{5.812 - ln\left(1 + \frac{\psi}{3000}\right)}{5.812} \right] \quad (5)$$

In the above equation, $\theta_s$ (39%) is saturated volumetric water content and $a$ (1,550 kPa), $n$ (0.4), and $m$ (2.3) are fitting parameters. The investigated sample showed an air entry value (AEV) of 300 kPa and a residual suction value (RSV) of 3 × $10^4$ kPa. The mild slope up to AEV is due to drainage of water from relatively bigger pores whereas the steep slope thereafter is due to water removal from comparatively smaller pores. This behavior is typical of compacted clays showing a wide range of pore sizes (Leroueil and Hight, 2013; Chen et al., 2019). Beyond RSV, the curve gradually reached complete desaturation ($\theta$ = 0%) at $10^6$ kPa. Furthermore, the measured saturated hydraulic conductivity ($k_s = 10^{-10}$ m/s) along with WRC was used to estimate the HCC (Figure 2b) using the following equation (Leong and Rahardjo, 1997):

$$k_u = k_s \left\{ \left\{ \frac{1}{ln\left[2.718 + \left(\frac{\psi}{a}\right)^n\right]^m} \right\} \left[ \frac{5.812 - ln\left(1 + \frac{\psi}{3000}\right)}{5.812} \right] \right\}^p \quad (6)$$

In the above equation, $p$ (5.5) is a new fitting parameter along with $a$, $n$, and $m$ carried forward from WRC. Similar to WRC, the HCC consisted of three zones (Chen et al., 2019; Ito and Azam, 2020): saturated flow up to AEV; unsaturated flow occurs between AEV and RSV; and vapor flow beyond RSV (Ebrahimi-Birang et al., 2004).

The volumetric water content curve for unfrozen water in clays (Flerchinger et al., 2006) was normalized (Figure 2c) and the data were found to best the following hyperbolic equation:

$$\theta_w = \frac{-0.154}{T} \times 100\% \quad (7)$$

Likewise, the values of thermal conductivity for frozen conditions (4.53 W/(m·°C)) and unfrozen conditions (2.97 W/(m·°C)) were obtained from the mineral composition of the investigated clay using the procedure given in Côté and Konrad (2005). The thermal conductivity function (Figure 2d) was drawn between the extreme values using the estimation method of Johansen (1975), and the data were found to best fit the following hyperbolic equation:

$$K_T = \frac{0.117}{T} + 4.55 \quad (8)$$

Finally, the volumetric heat capacity values under frozen conditions (2050 kJ/($m^3$·°C)) and unfrozen conditions (2850 kJ/($m^3$·°C)) for clay were obtained from Pavon (2018).

### 3.2. Atmospheric Parameters

Figure 3 presents the annual average atmospheric parameters based on 2011 ~ 2020 data for Saskatoon, Canada (Canada Weather Stats, 2021; Saskatchewan Research Council, 2021). The daily data were statistically analyzed to obtain mean values. Based on the mean data, the daily standard deviation was calculated to obtain the 95% confidence interval for each parameter of the five parameters. This means that the dry condition corresponded to the combined atmospheric parameters of low $q_p$, high $T_a$, low $h_a$, high $U_a$, and high $q_n$ and the wet condition matched with the reverse of dry conditions. Other possible combinations resulting in dry and wet conditions were not considered. The one-year period was divided into two seasons based on the mean soil temperature at the surface (given later in this paper): spring-summer (April to October) corresponding to more than 0 °C and fall-winter (November to March) with less than 0 °C. Furthermore, the relevant parameters were used to compute daily evaporation as per Equation 2. The cumulative monthly precipitation and evaporation were used to compute the standardized precipitation evapotranspiration index (SPEI) in R software following the method described in Pei et al. (2020). The SPEI values were used to classify weather conditions as follows: dry (between −1.07 and −1.25), mean (between −0.16 and 0.12), and wet (between 1.10 and 1.24). According to Nam et al. (2015), the SPEI values are less than −1 for dry conditions, between −1 and 1 for mean conditions, and more than 1 for wet conditions.

The daily precipitation (Figure 3a) indicates that spring-summer rainfall occurs for 27 days (122 mm or 79% of the total) in dry conditions, 61 days (268 mm or 80% of the total) for mean conditions, and 118 days (482 mm or 93% of the total) for wet conditions. The remainder of the precipitation is in the form of snow that accumulates during fall-winter and melts during spring-summer when the air temperature is above 0 °C. Likewise, Figure 3b shows that the daily air temperature is above 0 °C for 350, 210, and 143 days for the above conditions. The high number of days with above 0 °C temperature correlates well with the semi-arid regional climate (Akhter and Azam, 2019; Shook and Pomeroy, 2016). Using the Köppen-Geiger climate classification system (Kottek et al., 2006), the atmospheric parameters for dry and mean conditions were found to be cold desert climate (BWk) whereas the wet condition was classified as cold arctic climate (Dfc).

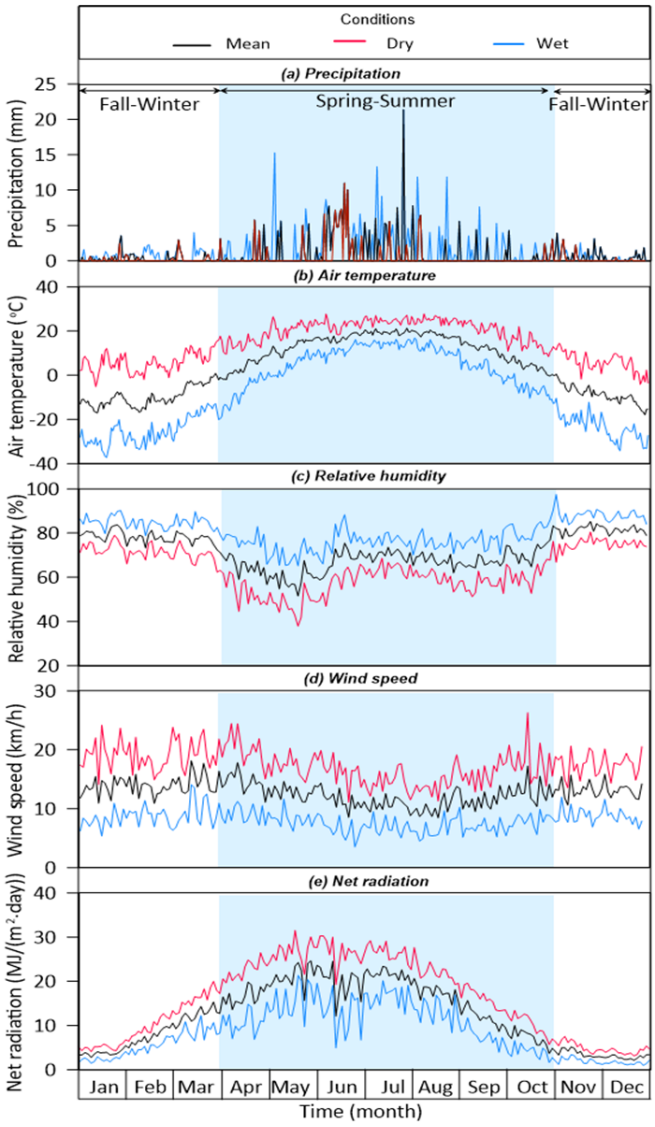


**Figure 3.** Daily variation of the atmospheric parameter in Saskatoon, Canada: (a) precipitation; (b) air temperature; (c) relative humidity; (d) wind speed; and (e) net radiation.

The daily relative humidity (Figure 3c) during spring-summer showed an average value of 57% for dry condition, 67% for mean condition, and 76% for wet condition. These average values increase during fall-winter to 73, 81, and 86%, respectively. The daily wind speed (Figure 3d) for the same conditions fluctuates irrespective of the seasons and shows an annual average of 22, 17, and 11 km/h, respectively. The daily net radiation (Figure 3e) shows a spring-summer average of 22 MJ/(m$^2$·day) for dry condition, 17 MJ/(m$^2$·day) for mean condition, and 12 MJ/(m$^2$·day) for wet condition whereas the corresponding fall-winter averages were 7, 4, and 3 MJ/(m$^2$·day). These daily atmospheric parameters corresponding to each condition were applied directly to the model whereas the snow accumulation or melting was estimated based on precipitation and air temperature.

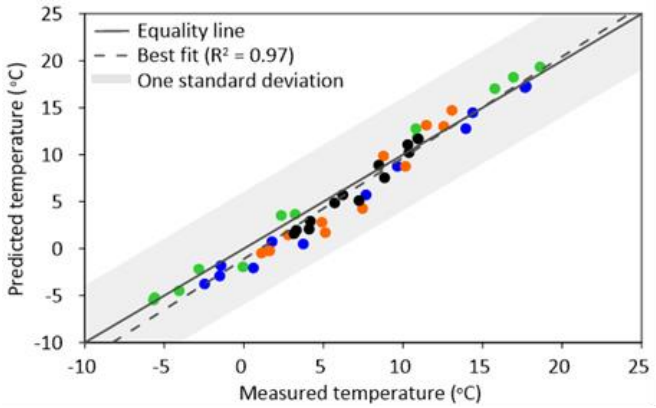


**Figure 4.** Comparison of predicted and measured monthly soil temperatures.

### 3.3. Soil Temperature

A constant soil temperature of 7 °C at 8 m was used. This was based on 2011 ~ 2020 data of measured soil temperature profile for the Saskatoon area (Saskatchewan Research Council, 2021). According to Lebeau and Konrad (2009), the fluctuations of air temperature on glacial clay deposits do not affect soil temperature beyond 6 m depth.

## 4. Results and Discussion

To determine the effectiveness of prediction, the coupled thermal-hydraulic model was validated by comparing the predicted and measured daily temperature profiles. Figure 4 compares the monthly predicted and measured soil temperature. The predicted temperatures were almost equal to the measured temperatures with a coefficient of determination ($R^2$) higher than 0.97, mean absolute error (MAE) between 0.95 and 1.80, and root mean squared error (RMSE) between 1.10 and 1.95 for all depths. The data are plotted on both sides of the equality line and entirely fell within one standard deviation. This confirms that the model is appropriately calibrated for the regional soil properties and climatic conditions. This validation is based on field data at a specific station, which is the only one in the region with soil properties similar to the investigated clay. Such soils are widely found across the Canadian Prairies with the following conductivities: $k_s$ ranges from $10^{-9}$ m/s to $10^{-11}$ m/s (Vanapalli et al., 1997; Ferris et al., 2020; Paranthaman and Azam, 2021b) and $K_T$ varies from 2 to 5 W/(m·°C) (Côté and Konrad, 2005; Lebeau and Konrad, 2009; Pavon, 2018). Given that the investigated soil properties fall within these ranges along with the capture of a wide range of climatic conditions, the model is applicable for the entire region.

Figure 5 shows the variation of soil temperature with respect to time. To obtain continuous data, daily predictions are plotted versus monthly measurement at 0.05, 0.5, 1.5, and 3 m depths. Following air temperature, soil temperature exhibited a cyclic trend for all depths such that daily fluctuations decreased with depth. Soil temperature at 0.05 m depth closely matched the air temperature during spring-summer and was found to be

half of the latter during fall-winter. This is because heat flow from soil to air makes the ground surface warmer than air under sub-zero temperature (Cinar et al., 2020; Zhang et al., 2020). Furthermore, the curves shift towards the right side with each depth increment. This time lag is attributed to the transient process of thermal conduction and isolation of the deeper layers from the atmosphere (Le et al., 2020).

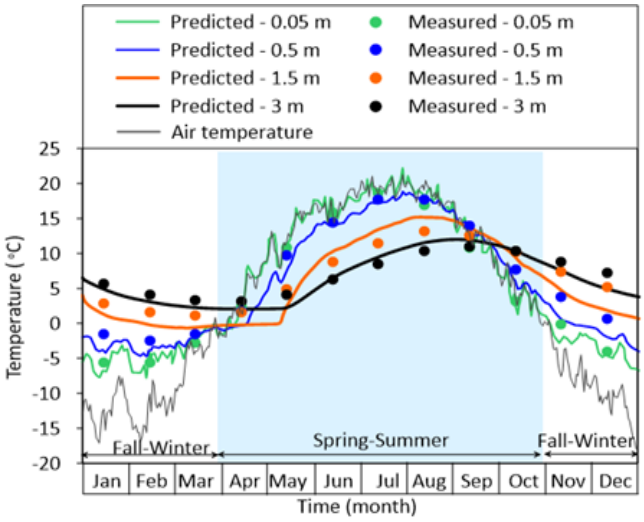


**Figure 5.** Variation of predicted and measured soil temperatures with time.

Figure 6 shows the variation of cumulative fluxes at the soil-atmosphere interface with the negative sign for outflow and the positive sign for inflow. Under mean conditions (Figure 6a), the net flux was found to be negative because of a net water deficit due to the semi-arid climate of the region. The average annual precipitation (based on Figure 3) was found to be 342 mm compared to the average annual pan evaporation of 377 mm (Golder associates, 2013). The variation in net flux was found to comprise the following: no change from January to mid-April (due to 35 mm of snow accumulation and frozen soil surface); a decrease from mid-April to mid-May (due to 133 mm of actual evaporation despite melting of snow); a gradual decrease from mid-May to October (since actual evaporation (290 mm) exceeded rainfall (240 mm)); and no change from November to December (due to snow cover of 38 mm and frozen soil surface). The runoff was found to be negligible because of a water deficit prevalent throughout the year. Based on hydraulic flow, four distinct seasons of winter (3½ months), spring (1 month), summer (5½ months), and fall (2 months) were observed. This correction of the seasons (based on water fluxes) is more relevant to shallow geothermal energy assessment, as opposed to that based on air temperature only.

Under dry conditions (Figure 6b), net flux was found to be negative due to high actual evaporation (annual total of 408 mm or 133% of the mean conditions) and low precipitation (annual total of 153 mm or 45% of the mean conditions). Such long-term droughts are common in the region, for example, early 1970s, 1980s and from 1999 to 2005 (Bonsal et al., 2011; Mood et al., 2021). In contrast to the mean conditions, the net flux decreased from January to April because under above-zero air temperature precipitation occurred as rainfall (27 mm) which is almost one order of magnitude lower than actual evaporation (252 mm). This is followed by a slight increase from May to August (because rainfall of 109 mm significantly exceeds actual evaporation of 10 mm) and a subsequent gradual decrease from September to December (because actual evaporation (152 mm) was almost ten times more than precipitation (16 mm)). As expected, the runoff was found to be zero owing to a net water deficit. In contrast to the mean conditions, this figure shows that the margins of the seasons are shifted to the left showing no winter, longer spring (4 months), shorter summer (4 months), and longer fall (4 months).

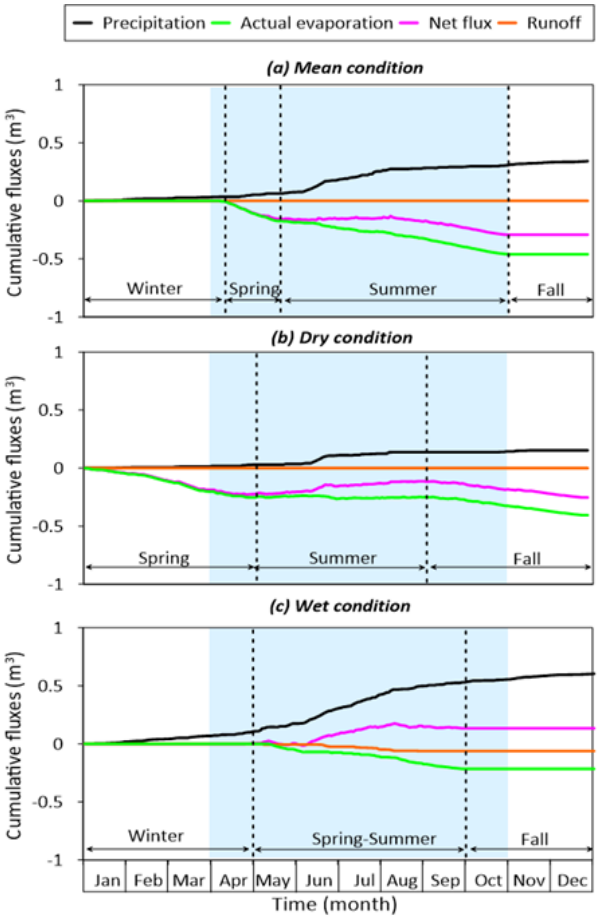


**Figure 6.** Cumulative water fluxes under various climatic conditions: (a) mean; (b) dry; and (c) wet.

Under wet conditions (Figure 6c), net flux remained mostly positive because precipitation (annual total of 605 mm or 178% of the mean conditions) exceeds actual evaporation (annual total of 215 mm). Such conditions can be brought about by flash floods, for example, in 2011, 2013, and 2014 (Shook and Pomeroy, 2016). The net flux exhibited no change from January to April because of a thick snow cover (due to high precipitation of 107 mm) and frozen soil surface (due to sub-

zero air temperature). This is followed by a gradual increase from May to September (because rainfall (425 mm) was more than twice the actual evaporation (211 mm)) and then by a negligible change from October to December (due to freezing of soil surface and snow cover under sub-zero air temperature). The runoff exhibited a low decrease because high water infiltration into the ground despite of high meltwater and high rainfall. In relation to the mean conditions, this figure shows three seasons of winter (4 months), inseparable spring-summer (5 months), and a longer fall (3 months).

Figure 7 presents the variation of hydraulic properties with respect to time in the form of degree of saturation and soil suction from the surface to 8 m depth at 1 m increments. All plots start from the initial values ($S$ = 80% and $\psi$ = 100 kPa) corresponding to optimum compaction and follow the net flux trends given in Figure 6 such that the fluctuations were high close to the surface and decreased with depth. This is because the ground surface is directly exposed to the atmosphere and water movement in successive soil layers is governed by the variations in unsaturated hydraulic conductivity. Under mean conditions (Figures 7a and 7d), both $S$ and $\psi$ remained constant (80% and 40 kPa) from January to mid-April, varied between 20 and 80% corresponding to $7 \times 10^4$ and 40kPa from mid-May to October, and converged to 70% (400 kPa) during November to December. Under dry conditions (Figures 7b and 7e), these parameters varied between 76 and 18% (100 to $10^5$ kPa) from January to August and converged at $S$ = 60% and $\psi = 10^3$ kPa from September to December. Under wet conditions (Figures 7c and 7f), both $S$ and $\psi$ remained constant (80% and 40 kPa) from January to April, fluctuated between 95% (10 kPa) and 60% (700 kPa) from May to September, and bounced back to constant values of $S$ = 80% and $\psi$ = 40 kPa from October to December.

During fall and winter, unsaturated hydraulic flow is primarily driven by soil suction and is further restricted because of frozen soil and snow cover. With the downward migration of sub-zero temperature, the hydraulic flow is further reduced due to the formation of ice by attracting pore water from the soil (Konrad and Samson, 2000). During spring and summer, water is in the form of liquid and vapor within the soil pores and, as such, unsaturated hydraulic flow is governed by alternate evaporation and infiltration. When the soil is desiccated (that is, more than RSV of $3 \times 10^4$ kPa), vapor flow is the dominant mechanism of hydraulic transport (Ebrahimi-Birang et al., 2004). Given the unsaturated condition of the soil along with freezing in fall and winter and extreme dryness during summer, heat conduction is expected to be hindered.

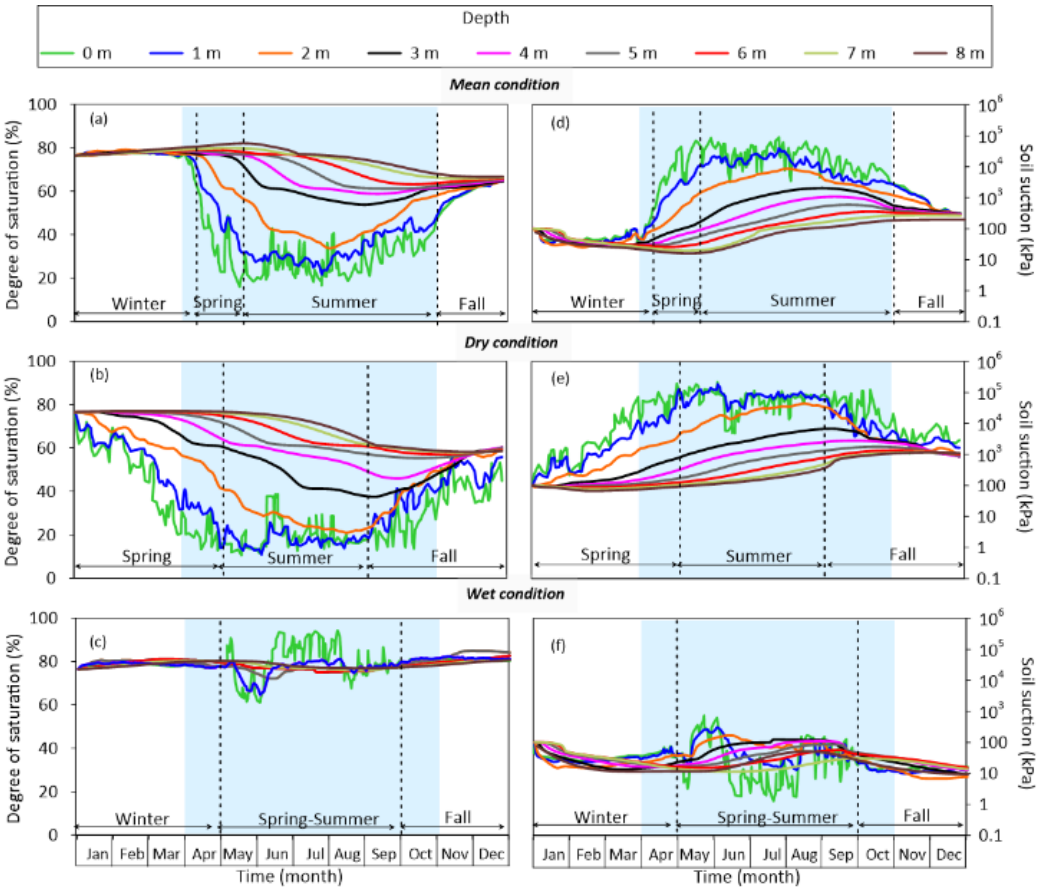


**Figure 7.** Variation of hydraulic properties: degree of saturation under various conditions: (a) mean; (b) dry; and (c) wet as well as soil suction under various conditions: (d) mean; (e) dry; and (f) wet.

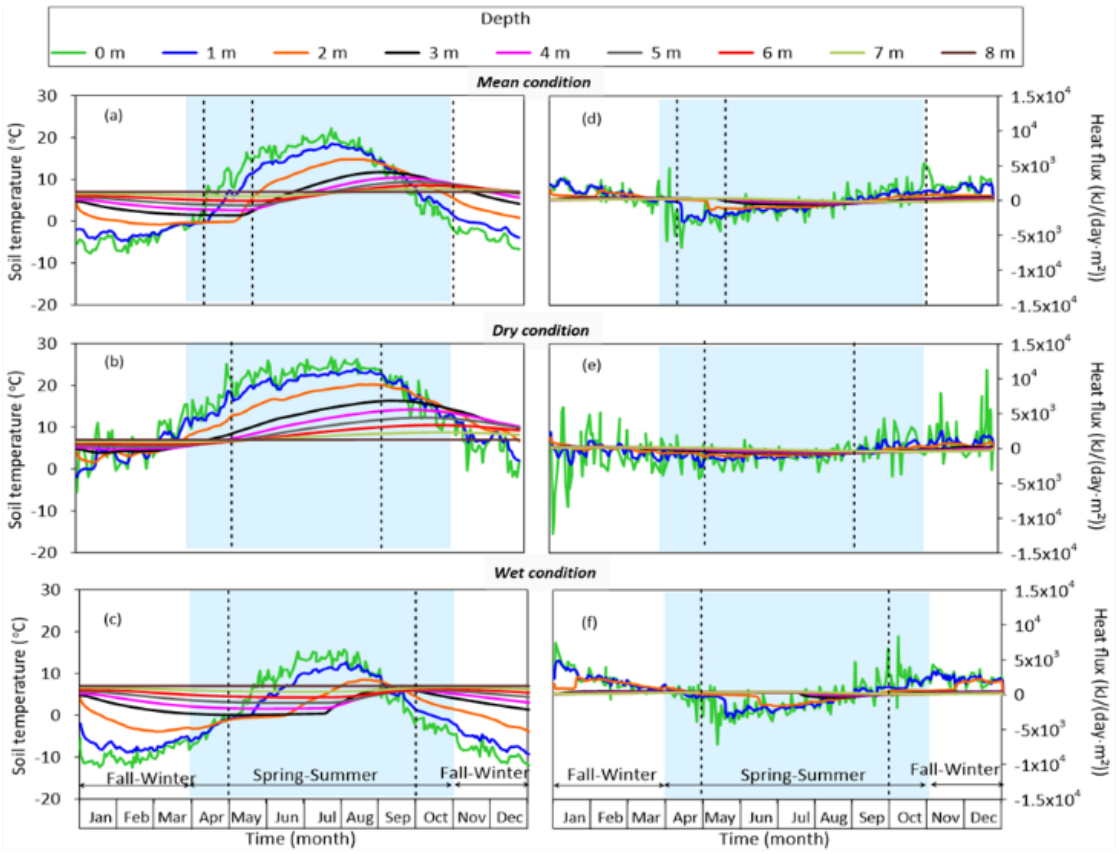


**Figure 8.** Variation of thermal properties: soil temperture under various conditions: (a) mean; (b) dry; and (c) wet as well as heat flux under various conditions: (d) mean; (e) dry; and (f) wet.

Figure 8 shows the variation of thermal properties with respect to time in the form of soil temperature and heat flux from the surface to 8 m depth at 1 m increments. The soil temperature plots followed the cyclic trend of air temperature (Figure 3b) with high fluctuations at the surface that gradually diminished with depth. The $T_s$ was found to be above 0 °C throughout the year at and beyond 3.0 m depth. This coincides with the frost depth of 1.8 m (Clifton Associates, 2009) in regional soils validates the model and the use of seasonal boundaries in Figure 3b. During fall-winter, the $T_s$ values varied by 14 degrees for the mean (−7 to 7 °C) and the dry (−2 to 12 °C) conditions and by 19 degrees (−12 to 7 °C) for the wet weather. These values indicate that the soil loses heat during fall-winter such that this loss is more predominant under wet conditions. During spring-summer, the $T_s$ values varied by 20 ± 2 degrees for all scenarios (0 to 20 °C for mean, 7 to 25 °C for dry, and −7 to 15 °C for wet weather). These identical values of thermal gradient (soil temperature change divided by soil depth) suggest that the soil gains heat during spring-summer irrespective of the weather scenarios. Such a heat gain is expected to be more than the heat loss during fall-winter because of the lower gradients during this time.

The daily heat flux ($q_g$) plots showed high fluctuations of heat dissipation (positive) and heat recharge (negative) at the surface. The surface variations were found to be low for mean conditions (4,300 to −6,050 kJ/(day·m$^2$)) and wet conditions (7,780 to −6,050 kJ/(day·m$^2$)) when compared with dry conditions (11,200 to −12,100 kJ/(day·m$^2$)). Such fluctuations gradually decreased with depth because of a decrease in the thermal gradient over the soil profile. Irrespective of the seasonal boundaries, the heat flux showed an initial inflection point from positive to negative in April (that is, soil loses heat from September to April) and a final inflection point from negative to positive in August (that is, soil gains heat from May to August). These inflection points were found to be distinct under mean and wet conditions and fuzzy under dry conditions.

During fall and winter, the ice front grows from the top downwards because of high values of $K_T$ (4.5 W/(m·°C)) and $\theta_w$ (10 ± 5%) thereby resulting in heat loss through soil particles and ice crystals (Newman and Wilson, 1997). Furthermore, the development of ice front facilitates an upward movement of pore water from the remainder of the soil. This further decreases the degree of saturation such that heat loss primarily occurs through soil particles (Konrad and Samson, 2000). During spring and summer, heat flow takes place at and above 0 °C for which $K_T$ (3.0 W/(m·°C)) and $\theta_w$ (100%). According to Côté and Konrad (2005), heat flow under such conditions is driven by alternate saturation (soil particles and water-filled pores) and desaturation (soil particles and partially water-filled pores).

**Table 1.** Summary of Hydraulic and Thermal Band Boundaries during the Investigated Year

| Depth (m) | $S$ (%) | | $\psi$ (kPa) | | $T_s$ (°C) | | $q_g$ (kJ/(day·m$^2$)) | |
|---|---|---|---|---|---|---|---|---|
| | Min | Max | Min | Max | Min | Max | Min | Max |
| *Mean conditions* | | | | | | | | |
| 0 | 18 | 80 | 40 | 70,000 | −7 | 21 | −3,700 | 3,700 |
| 1 | 28 | 80 | 40 | 20,000 | −3 | 17 | −1,900 | 1,900 |
| 2 | 40 | 80 | 40 | 7,000 | 0 | 14 | −780 | 780 |
| 3 | 54 | 80 | 40 | 2,000 | 2 | 12 | −520 | 520 |
| 4 | 58 | 80 | 40 | 1,000 | 3 | 10 | −400 | 400 |
| 5 | 62 | 80 | 40 | 700 | 4 | 10 | −260 | 260 |
| 6 | 64 | 80 | 40 | 300 | 5 | 89 | −260 | 260 |
| 7 | 65 | 80 | 40 | 200 | 6 | 8 | −260 | 260 |
| 8 | 66 | 80 | 40 | 200 | 7 | 7 | −260 | 260 |
| *Dry Conditions* | | | | | | | | |
| 0 | 8 | 76 | 100 | 400,000 | −2 | 26 | −8,600 | 6,900 |
| 1 | 16 | 76 | 100 | 80,000 | 0 | 22 | −1,700 | 1,000 |
| 2 | 26 | 76 | 100 | 20,000 | 3 | 19 | −860 | 520 |
| 3 | 35 | 76 | 100 | 7,000 | 4 | 17 | −690 | 390 |
| 4 | 46 | 76 | 100 | 3,000 | 5 | 14 | −520 | 260 |
| 5 | 56 | 76 | 100 | 2,000 | 6 | 13 | −520 | 260 |
| 6 | 57 | 76 | 100 | 1,000 | 6 | 11 | −520 | 260 |
| 7 | 58 | 76 | 100 | 1,000 | 7 | 9 | −520 | 260 |
| 8 | 58 | 76 | 100 | 1,000 | 7 | 7 | −520 | 260 |
| *Wet Conditions* | | | | | | | | |
| 0 | 62 | 90 | 4 | 500 | −12 | 16 | −4,800 | 5,200 |
| 1 | 68 | 87 | 6 | 190 | −6 | 10 | −2,400 | 3,500 |
| 2 | 73 | 85 | 7 | 150 | −2 | 7 | −1,000 | 1,800 |
| 3 | 75 | 82 | 10 | 110 | 0 | 6 | −260 | 780 |
| 4 | 76 | 81 | 11 | 100 | 2 | 6 | 0 | 520 |
| 5 | 76 | 81 | 11 | 100 | 3 | 6 | 0 | 520 |
| 6 | 76 | 81 | 11 | 100 | 4 | 6 | 0 | 520 |
| 7 | 76 | 81 | 11 | 100 | 6 | 7 | 0 | 520 |
| 8 | 76 | 81 | 11 | 100 | 7 | 7 | 0 | 520 |

Table 1 summarizes the hydraulic and thermal properties through the soil profile with Figure 9 showing the hydraulic properties and Figure 10 illustrating the thermal properties. The $S$ and $\psi$ plots (Figure 9) show bands between the minimum and the maximum values with a larger range at the exposed surface that gradually narrowed down with depth due to the increasing soil cover. Under mean conditions, the plots showed a half funnel-shaped trend with the maximum $S$ (minimum $\psi$) of 80% (40 kPa) throughout the soil column. The minimum $S$ (maximum $\psi$) was found to be 18% (70,000 kPa) at the surface, followed by a gradual increase to 58% (1,000 kPa) at 4 m, and then remained constant at about 65% (200 kPa). Under dry conditions, the trend was found to be similar to the mean with the maximum $S$ (minimum $\psi$) of 76% (100 kPa) over 8 m depth. The corresponding values for the minimum $S$ (maximum $\psi$) were 8% (400,000 kPa) at the surface, 56% (2,000 kPa) at 5 m, and 58% (1,000 kPa) thereafter. In contrast, the trend was found to be funnel-shaped under wet conditions with $S$ of 90% (4 kPa) to 62% (500 kPa) at the surface, gradually decreasing to 82% (10 kPa) and 75% (110 kPa) at 3 m and remained constant thereafter. These data indicate that 4 ± 1 m is the active depth (showing significant variation in behavior) of soil where hydraulic properties are governed by soil-atmosphere interactions.

The $T_s$ and $q_g$ (Figure 10) show funnel-shaped bands with broad ranges near the exposed surface that gradually decreased with depth due to increasing soil cover. Under mean conditions, symmetrical trends were observed with $T_s$ ranging from −7 °C to 21 °C at the surface and gradually decreased to 7 °C at 8 m. Likewise, $q_g$ varied over ± 3,700 kJ/(day·m$^2$) at the surface and steadily reached ±400 kJ/(day·m$^2$) at 4 m, and remained constant subsequently. Under dry conditions, the trend of $T_s$ shifted towards the right with $T_s$ varying from −2 to 26 °C at the surface and reaching 7 °C at 8 m depth. The corresponding $q_g$ trend was much wider with a range of −8,600 to 6,900 kJ/(day·m$^2$) at the surface that narrowed down to varied between −690 and 390 kJ/(day·m$^2$) at 3 m and remained constant thereafter. Under wet conditions, the trend of $T_s$ shifted to the left with $T_s$ range of 16 to −12 °C at the surface that progressively decreased to 7 °C over 8 m depth. The $q_g$ was found to be between −4,800 and 5,200 kJ/(day·m$^2$) at the surface and consistently approached to range from −260 to 780 kJ/(day·m$^2$) at 3 m and remained constant afterward. These data indicate that 3 m is the active depth of soil where heat flux is governed by soil-atmosphere interactions.

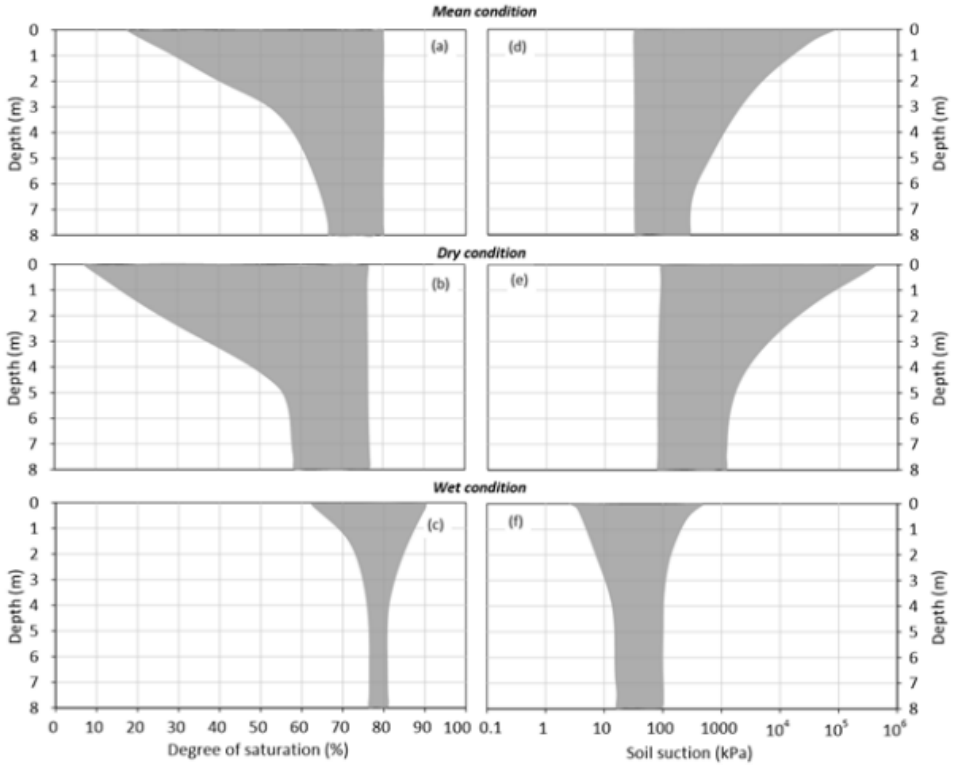


**Figure 9.** Band of hydraulic profiles during the investigated year: degree of saturation under various conditions: (a) mean; (b) dry; and (c) wet as well as soil suction under various conditions: (d) mean; (e) dry; and (f) wet.

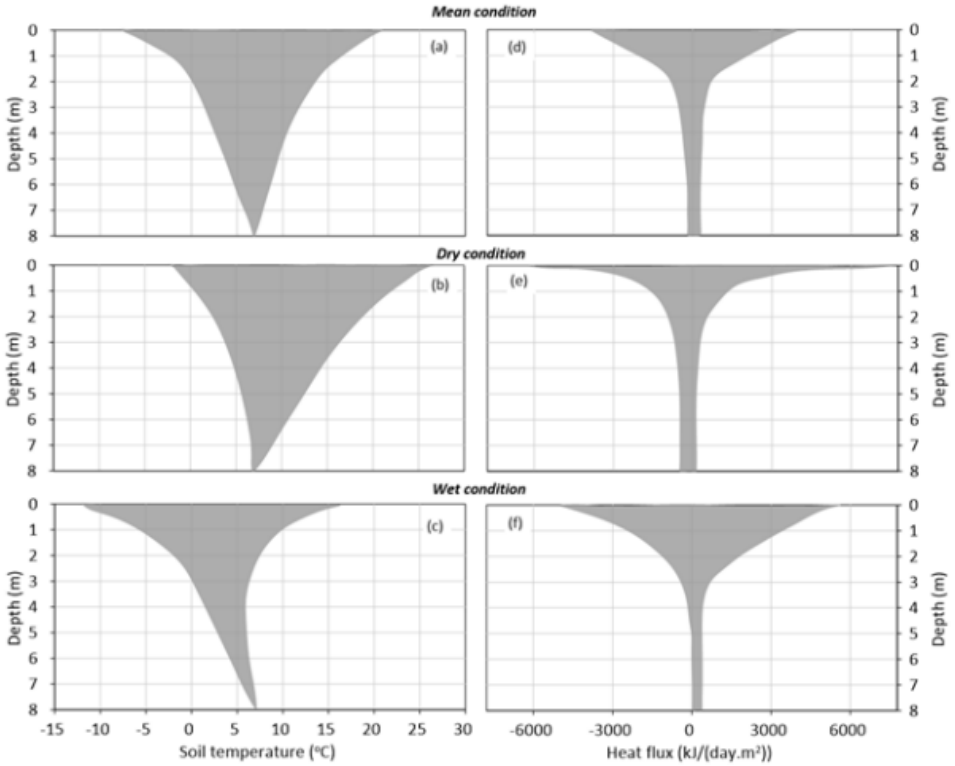


**Figure 10.** Band of thermal profiles during the investigated year: soil temperature under various conditions: (a) mean; (b) dry; and (c) wet as well as heat flux under various conditions: (d) mean; (e) dry; and (f) wet.

The coupled model provides a baseline for understanding the hydraulic and thermal properties of soils under extreme weather in cold regions. The model demonstrates that 5 m is the active depth for buried infrastructure under all climatic conditions including mean, extreme dry, and extreme wet. The following areas need to be further explored to ensure the successful installation and operation of buried facilities: (i) heat dissipation and absorption through the soil from the pipeline; (ii) system insulation due to vegetation and/or structural cover; (iii) impact of frozen water and built-up of pressure inside the pipes; (iv) applied stress by traffic and structural loads; and (v) long-term durability of the pipelines under climate changes.

## 5. Summary and Conclusion

The unique regional features of glacial geology (resulting in clay deposits) and extreme weather conditions (resulting in flash-floods and long-droughts) in southern Saskatchewan (Canada) govern the hydraulic and thermal properties of soil deposits. A coupled soil-atmospheric model was developed to predict transient water and heat movement under mean, extreme dry, and extreme wet weather scenarios. The primary achievement of this research is that the proposed numerical model is capable of determining soil behavior with respect to both time and depth. The main conclusions of this research are summarized as follows:

- The hydraulic properties are governed by the net flux between precipitation and evaporation that resulted in the shifting of the seasons under various scenarios: mean comprising winter (3½ months), spring (1 month), summer (5½ months), and fall (2 months); dry comprising spring (4 months), summer (4 months), and fall (4 months); and wet comprising winter (4 months), inseparable spring-summer (5 months), and fall (3 months). The active depth of soil was found to be 4 ± 1 m, where hydraulic properties are governed by soil-atmosphere interactions.
- The thermal properties are governed by air temperature for the investigated soil. Identical values of thermal gradient during longer spring-summer (April to October) in all scenarios indicate that the soil gains more heat compared with the heat lose during shorter fall-winter (November to March), especially for mean and dry conditions. The inflection points in heat flux showed that the soil gains heat from May to August and loses heat from September to April. A 3 m depth was found to be the active soil zone where heat flux is affected by soil-atmosphere interactions.

**Author Contributions.** Conceptualization, S.A.; Data curation, R.P.; Formal analysis, R.P.; Funding acquisition, S.A.; Investigation, R.P.; Supervision, S.A.; Writing—original draft, R.P.; Writing—review & editing, S.A. All authors have read and agreed to the published version of the manuscript.

**Funding.** This research was funded by Natural Sciences and Engineering Research Council of Canada, grant number RGPIN-06456-2018.

**Data Availability Statement.** The data presented in this study are available in the figures and tables.

**Acknowledgments.** The authors would like to acknowledge the University of Regina for providing laboratory space and computing facilities.

**Conflicts of Interest.** The authors declare no conflict of interest.

## References

Akhter, A. and Azam, S. (2019). Flood-Drought Hazard Assessment for a Flat Clayey Deposit in the Canadian Prairies. *Journal of Environmental Informatics Letters*. 1(1), 8-19. https://doi.org/10.3808/JEIL.201900002

Azam, S., Shah, I., Raghunandan, M.E. and Ito, M. (2013). Study on swelling properties of an expansive soil deposit in Saskatchewan, Canada. *Bulletin of Engineering Geology and the Environment*. 72(1), 25-35. https://doi.org/10.1007/s10064-012-0457-0

Bittelli, M., Campbell, G.S. and Tomei, F. (2015). *Soil physics with Python: Transport in the soil-plant-atmosphere system*. Oxford Scholarship Online. https://doi.org/10.1093/acprof:oso/9780199683093.001.0001

Bonsal, B.R., Cuell, C., Wheaton, E., Sauchyn, D.J. and Barrow, E. (2017). An assessment of historical and projected future hydroclimatic variability and extremes over southern watersheds in the Canadian Prairies. *International Journal of Climatology*. 37(10), 3934-3948. https://doi.org/10.1002/joc.4967

Bonsal, B.R., Wheaton, E.E., Chipanshi, A.C., Lin, C., Sauchyn, D.J. and Wen, L. (2011). Drought research in Canada: A review. *Atmosphere-Ocean*. 49(4), 303-319. https://doi.org/10.1080/07055900.2011.555103

Canada Weather Stats. https://www.weatherstats.ca/ (accessed August 21, 2021).

Chen, R.P., Liu, P., Liu, X.M., Wang, P.F. and Kang, X. (2019). Pore-scale model for estimating the bimodal soil-water characteristic curve and hydraulic conductivity of compacted soils with different initial densities. *Engineering Geology*. 260, 105199. https://doi.org/10.1016/j.enggeo.2019.105199

Çinar, A., Sun, X., Soga, K., Nico, P. and Dobson, P. (2020). City-Scale Modeling of San Francisco Bay Area Underground for Community-Scale Application of Geothermal Energy. *Community Resilience through Low Temperature Geothermal Reservoir Thermal Energy Storage, 45th Workshop on Geothermal Reservoir Engineering*, California, 10-12.

City of Regina. City of Regina | Home. https://www.regina.ca/ (accessed June 10th, 2022).

City of Winnipeg. Water Main Cleaning Schedule-Water-Water and Waste-City of Winnipeg. City of Winnipeg Water and Waste Water Department's Water Main Activity Page. https://winnipeg.ca/waterandwaste/water/watermainactivities.asp#8 (accessed June 10, 2022).

Clifton Associates Ltd. (2009). *Saskatchewan Multi-Use Facility Feasibility Study*. File R4397.

Côté, J. and Konrad, J.M. (2005). A generalized thermal conductivity model for soils and construction materials. *Canadian Geotechnical Journal*. 42(2), 443-458. https://doi.org/10.1139/t04-106

Dall'Amico, M., Endrizzi, S., Gruber, S. and Rigon, R. (2011). A robust and energy-conserving model of freezing variably-saturated soil. *The Cryosphere*. 5, 469-484. https://doi.org/10.5194/tc-5-469-2011

Ebrahimi-B, N., Gitirana Jr, G.F.N., Fredlund, D.G., Fredlund, M.D. and Samarasekera, L. (2004). A lower limit for the water permeability coefficient. *Saturated/Unsaturated Constitutive Modelling · Saturated/Unsaturated Groundwater Seepage, 57th Canadian Geotechnical Conference*, Quebec City, 24-27.

Ferris, D.M., Potter, G. and Ferguson, G. (2020). Characterization of the hydraulic conductivity of glacial till aquitards. *Hydrogeology*

*Journal*. 28, 1827-1839. https://doi.org/10.1007/s10040-020-02161-7

Flerchinger, G.N., Seyfried, M.S. and Hardegree, S.P. (2006). Using soil freezing characteristics to model multi-season soil water dynamics. *Vadose Zone Journal*. 5(4), 1143-1153. https://doi.org/10.2136/vzj2006.0025

Fredlund, D.G. and Xing, A.Q. (1994). Equations for the soil-water characteristic curve. *Canadian Geotechnical Journal*. 31(4), 521-532. https://doi.org/10.1139/t94-061

Fukuda, M., Orhun, A. and Luthin, J.N. (1980). Experimental studies of coupled heat and moisture transfer in soils during freezing. *Cold Regions Science and Technology*. 3(2-3), 223-232. https://doi.org/10.1016/0165-232X(80)90028-2

Geostudio. (2020). *Heat and mass transfer modeling with GeoStudio 2020 (First Edition)*. Geostudio International Ltd.

Golder associates. (2013). *Tazi Twé Hydroelectric Project*. Elizabeth Falls, Saskatchewan, CA.

Green, W.H. and Ampt, G.A. (1911). Studies on Soil Phyics. *The Journal of Agricultural Science*. 4(1), 1-24. https://doi.org/10.1017/S0021859600001441

Harlan, R.L. (1973). Analysis of coupled heat-fluid transport in partially frozen soil. *Water Resources Research*. 9(5), 1314-1323. https://doi.org/10.1029/WR009i005p01314

Hillel, D. (1998). *Environmental soil physics: Fundamentals, applications, and environmental considerations*. Elsevier.

Hu, Y.F. and Vu, H.Q. (2006). Field performance of water mains buried in expansive soil. *Water mains, 1st International Structural Specialty Conference (CSCE 2006)*, Calgary, 1-13.

Hu, Y.F. and Vu, H.Q. (2011). Analysis of soil conditions and pipe behaviour at a field site. *Canadian Geotechnical Journal*. 48(6), 847-866. https://doi.org/10.1139/t11-010

Hu, Y.F., Vu, H.Q. and Lotfian, K. (2008). Instrumentation of a section of AC pipe in expansive soil, *International Pipelines Conference*, Atlanta, 1-10.

Huang, S.B., Guo, Y.L., Liu, Y.Z., Ke, L.H., Liu, G.F. and Chen, C. (2018). Study on the influence of water flow on temperature around freeze pipes and its distribution optimization during artificial ground freezing. *Applied Thermal Engineering*. 135, 435-445. https://doi.org/10.1016/j.applthermaleng.2018.02.090

Ito, M. and Azam, S. (2020). Relation between flow through and volumetric changes in natural expansive soils. *Engineering Geology*. 279, 105885. https://doi.org/10.1016/j.enggeo.2020.105885

Ito, M., Azam, S. and Clifton, W. (2022). Suction-based model for predicting cyclic and transient volume changes in expansive clays using a material property function. *Engineering Geology*. 296, 106491. https://doi.org/10.1016/j.enggeo.2021.106491

Johansen, O. (1975). *Thermal Conductivity of Soils*. Ph.D. Dissertation, Cold Regions Research and Engineering Laboratory, Hanover, New Hampshire., USA.

Kleiner, Y. and Rajani, B. (2002). Forecasting variations and trends in water-main breaks. *Journal of Infrastructure Systems*. 8(4), 122-131. https://doi.org/10.1061/(ASCE)1076-0342(2002)8:4(122)

Konrad, J.M. and Morgenstern, N.R. (1984). Frost heave prediction of chilled pipelines buried in unfrozen soils. *Canadian Geotechnical Journal*. 21(1), 100-115. https://doi.org/10.1139/t84-008

Konrad, J.M. and Samson, M. (2000). Influence of freezing temperature on hydraulic conductivity of silty clay. *Journal of Geotechnical and Geoenvironmental Engineering*. 126(2), 180-187. https://doi.org/10.1061/(ASCE)1090-0241(2000)126:2(180)

Kottek, M., Grieser, J., Beck, C., Rudolf, B. and Rubel, F. (2006). World Map of the Köppen-Geiger climate classification updated. *Meteorologische Zeitschrift*. 15(3), 259-263. https://doi.org/10.1127/0941-2948/2006/0130

Le, A.T., Wang, L., Wang, Y. and Li, D.L. (2020). Measurement investigation on the feasibility of shallow geothermal energy for heating and cooling applied in agricultural greenhouses of Shouguang City: Ground temperature profiles and geothermal potential. *Information Processing in Agriculture*. 8(2), 251-269 https://doi.org/10.1016/j.inpa.2020.06.001

Lebeau, M. and Konrad, J.M. (2009). Natural convection of compressible and incompressible gases in undeformable porous media under cold climate conditions. *Computers and Geotechnics*. 36(3), 435-445. https://doi.org/10.1016/j.compgeo.2008.04.005

Leong, E.C. and Rahardjo, H. (1997). Permeability functions for unsaturated soils. *Journal of Geotechnical and Geoenvironmental Engineering*. 123(12), 1118-1126. https://doi.org/10.1061/(ASCE)1090-0241(1997)123:12(1118)

Leroueil, S. and Hight, D.W. (2013). Compacted soils: From physics to hydraulic and mechanical behaviour. *Advances in Unsaturated Soils*. CRC Press, pp 41-59. https://doi.org/10.1201/b14393-8

Lowe, P.R. (1977). An Approximating Polynomial for the Computation of Saturation Vapor Pressure. *Journal of Applied Meteorology and Climatology*. 16(1), 100-103. https://doi.org/10. 1175/1520-0450(1977)016<0100:AAPFTC>2.0.CO;2

Lu, N. and Likos, W.J. (2004). *Unsaturated soil mechanics*. John Wiley and Sons, pp 369-389. ISBN: 978-0-471-44731-3

Mitchell, J.K. and Soga, K. (2005). *Fundamentals of soil behavior (Vol. 3)*. John Wiley & Sons, pp 255-269. ISBN: 978-0-471-46302-3

Mood, B.J., Bonsal, B., Howat, B. and Laroque, C.P. (2021). Multi-year white spruce drought legacies in southern Saskatchewan. *Forest Ecology and Management*. 491, 119144. https://doi.org/10.1016/j.foreco.2021.119144

Nam, W.H., Hayes, M.J., Svoboda, M.D., Tadesse, T. and Wilhite, D.A. (2015). Drought hazard assessment in the context of climate change for South Korea. *Agricultural Water Management*. 160, 106-117. https://doi.org/10.1016/j.agwat.2015.06.029

Newman, G.P. and Wilson, G.W. (1997). Heat and mass transfer in unsaturated soils during freezing. *Canadian Geotechnical Journal*. 34(1), 63-70. https://doi.org/10.1139/T96-085

Newport, R. (1981). Factors influencing the occurrence of bursts in iron water mains. *Water Supply and Management.* 3, 274-278.

(Derick) Nixon, J.F. (1991). Discrete ice lens theory for frost heave in soils. *Canadian Geotechnical Journal*. 28(6), 843-859. https://doi.org/10.1139/t91-102

Nowamooz, H., Nikoosokhan, S. and Chazallon, C. (2016). Seasonal thermal energy storage in shallow geothermal systems: Thermal equilibrium stage. *E3S Web of Conferences*, *3rd European Conference on Unsaturated Soils - "E-UNSAT 2016"*, Paris, 9, 6. https://doi.org/10.1051/e3sconf/20160907003

Padilla, F. and Villeneuve, J.P. (1992). Modeling and experimental studies of frost heave including solute effects. *Cold Regions Science and Technology*. 20(2), 183-194. https://doi.org/10.1016/0165-232X(92)90016-N

Paranthaman, R. and Azam, S. (2021a). Effect of Composition on Engineering Behavior of Clay Tills. *Geosciences*. 11(10), 427. https://doi.org/10.3390/geosciences11100427

Paranthaman, R. and Azam, S. (2021b). Effect of compaction on desiccation and consolidation behavior of clay tills. *Innovative Infrastructure Solutions*. 7, 31. https://doi.org/10.1007/s41062-021-00644-4

Pavon, G. (2018). *Evaluating the thermal properties of soils based on measured ground temperatures*. M.Sc. Dissertation, Department of Civil Engineering, University of Manitoba, Winnipeg, Manitoba., CA.

Pei, Z.F., Fang, S.B., Wang, L. and Yang, W.N. (2020). Comparative Analysis of Drought Indicated by the SPI and SPEI at Various Timescales in Inner Mongolia, China. *Water*. 12(7), 1925. https://doi.org/10.3390/w12071925

Qin, Z.P., Lai, Y.M., Tian, Y. and Zhang, M.Y. (2021). Stability behavior of a reservoir soil bank slope under freeze-thaw cycles in cold regions. *Cold Regions Science and Technology*. 181, 103181. https://doi.org/10.1016/j.coldregions.2020.103181

Rajani, B., Kleiner, Y. and Sink, J.E. (2012). Exploration of the

relationship between water main breaks and temperature covariates. *Urban Water Journal*. 9(2), 67-84. https://doi.org/10.1080/15730 62X.2011.630093

Saskatchewan Research Council. CRS Weather Summaries | Saskatchewan Research Council. https://www.src.sk.ca/climate-reference-stations/crs-weather-summaries (accessed June 10, 2022).

Shook, K. and Pomeroy, J.W. (2016). The effects of the management of Lake Diefenbaker on downstream flooding. *Canadian Water Resources Journal/Revue Canadienne Des Ressources Hydriques*. 41(1-2), 261-272. https://doi.org/10.1080/07011784.2015.1092887

Tan, X.J., Chen, W.Z., Tian, H.M. and Cao, J.J. (2011). Water flow and heat transport including ice/water phase change in porous media: Numerical simulation and application. *Cold Regions Science and Technology*. 68(1), 74-84. https://doi.org/10.1016/j.coldregions. 2011.04.004

Taylor, G.S. and Luthin, J.N. (1978). A model for coupled heat and moisture transfer during soil freezing. *Canadian Geotechnical Journal*. 15(4), 548-555. https://doi.org/10.1139/t78-058

Teslak, L. (2018). *Potential Microbial Water Quality Impacts Resulting from Main Breaks in Edmonton, Alberta: A Quantitative Microbial Risk Assessment*. M.Sc. Dissertation, School of Public Health, University of Alberta, Edmonton, Alberta, CA.

Tissen, C., Menberg, K., Bayer, P. and Blum, P. (2019). Meeting the demand: Geothermal heat supply rates for an urban quarter in Germany. *Geothermal Energy*. 7(1), 9. https://doi.org/10.1186/ s40517-019-0125-8

Tripathy, S. and Subba Rao, K.S. (2009). Cyclic Swell-Shrink Behaviour of a Compacted Expansive Soil. *Geotechnical and Geological Engineering*. 27(1), 89-103. https://doi.org/10.1007/ s10706-008-9214-3

Vanapalli, S.K., Fredlund, D.G. and Pufahl, D.E. (1997). Comparison of saturated-unsaturated shear strength and hydraulic conductivity behavior of a compacted sandy-clay till. *50th Canadian Geotechnical Conference*, Ottawa.

Vitel, M., Rouabhi, A., Tijani, M. and Guérin, F. (2016). Thermo-hydraulic modeling of artificial ground freezing: Application to an underground mine in fractured sandstone. *Computers and Geotechnics*. 75, 80-92. https://doi.org/10.1016/j.compgeo.2016.01.024

Wilson, G.W. (1990). *Soil evaporative fluxes for geotechnical engineering problems*. Ph.D. Dissertation, Department of Civil and Geological Engineering, University of Saskatchewan, Saskatoon, SK., CA.

Wilson, G.W., Fredlund, D.G. and Barbour, S.L. (1997). The effect of soil suction on evaporative fluxes from soil surfaces. *Canadian Geotechnical Journal*. 34(1), 145-155. https://doi.org/10.1139/t96-078

Yang, K. and Wang, C.H. (2019). Water storage effect of soil freeze-thaw process and its impacts on soil hydro-thermal regime variations. *Agricultural and Forest Meteorology*. 265, 280-294. https:// doi.org/10.1016/j.agrformet.2018.11.011

Zhang, Y.B., Zheng, J., Liu, A.H., Zhang, Q.L., Shao, J.L. and Cui, Y.L. (2020). Numerical Simulation of Shallow Geothermal Field in Operating of a Ground Source Heat Pump System-A Case Study in Nan Cha Village, Ping Gu District, Beijing. *Water*. 12(10), 2938. https://doi.org/10.3390/w12102938